Interaction of a free surface with a vortex patch

Christopher W. Curtis [a], Henrik Kalisch [b],*

[a] Department of Mathematics and Statistics, San Diego State University, San Diego, CA 92182, USA
[b] Department of Mathematics, University of Bergen, P.O. Box 7800, 5020 Bergen, Norway

HIGHLIGHTS

- Coupled discretization of a free surface and a vortex patch.
- Simultaneous evolution of a free surface and a distribution of point vortices.
- Fast implementation of Lagrangian–Eulerian regridding for the point vortices.
- Quantification of the influence of a free surface and a vortex patch on each other.

ARTICLE INFO

ABSTRACT

It is well known that most fluid flows feature vorticity. In order to avoid mathematical complexity, the study of surface waves is often carried out in the context of potential flow. In studies where vorticity is taken into account, it usually enters in a standard way, such as a background flow or in the boundary layer.

In the current contribution, a numerical method for the simulation of the simultaneous evolution of a free-surface wave and an existing vortex patch is developed. The method uses the formulation of the free-surface problem due to Ablowitz et al. (2006) in connection with point-vortex methods and numerical tools based on asymptotic development of the Dirichlet-to-Neumann operator for the free surface.

Simulations of shallow-water waves propagating over vortex patches of various strengths are then presented, and it is shown that the vortex patches can have strong, destabilizing effects on relatively low amplitude waves while their impact on surface profiles of larger amplitude is much weaker. It is also observed that very strong vortex patches are self-destabilizing when interacting with a free surface.

© 2019 Elsevier B.V. All rights reserved.

1. Introduction

The modeling of free-surface waves is a well studied and central area in several areas within applied mathematics, fluid mechanics and oceanography. Analytical concerns have motivated almost two-hundred years of work with a corresponding slew of techniques both formal and rigorous that have found use throughout applied mathematics. The free-surface problem also appears as a fundamental problem in both old [1] and modern [2] classics on fluid mechanics. Perhaps the greatest role that the problem plays though is in formulating the foundation for spectral-wave modeling, which forms the core of much of modern data-driven oceanography [3].

A long-standing question however in the modeling of free-surface waves is the impact that vorticity has on wave dynamics. This issue has been considered an especially difficult problem for general vorticity profiles given that the

---

* Corresponding author.
 E-mail addresses: ccurtis@mail.sdsu.edu (C.W. Curtis), henrik.kalisch@math.uib.no (H. Kalisch).
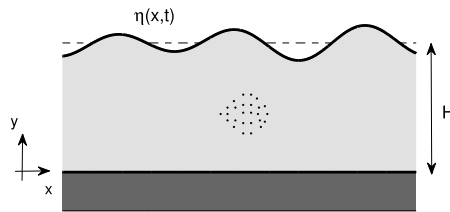
Fig. 1. Definition sketch and schematic of a vortex patch approximated by a number of point vortices. In reality hundreds of point vortices are used in the computations.

momentum equation cannot be readily integrated up to the surface via the use of a harmonic potential. Much progress has been made by making the simplifying assumption of the vorticity being constant leading to insightful numerical and analytic studies of these problems; see [4–6] among many others. In a similar vein, one can see the stability theory of shear profiles [7–9] as another means of addressing the impact of vorticity on free surface flows. This approach has been pushed to higher-order-nonlinear models with corresponding numerical implementations in [10].

However, in neither case can one track the evolution of an arbitrary vortex profile. As shown in experiment [11–13], the motion of solitary waves over bathymetric features induces the formation of vortex patches. Likewise, it is clear that accurate near shore modeling involves an understanding of the fluid vorticity profile and its interactions with the free surface. Progress in this direction has been made by assuming shallow-water scalings and deriving various Boussinesq-like models [14–16] or Green–Naghdi models [17–19]. These approaches, while limited to near-shore conditions, allow markedly enhanced modeling of shoaling and can be coupled to phenomenological models of wave-breaking induced turbulence to allow for very accurate near-shore computation.

In contrast to the above work, a body of numerical methods has been developed within computational fluid mechanics known as Point-Vortex Methods (PVMs). These are numerical schemes which track the evolution of compactly supported vorticity profiles via direct discretizations of the vorticity profile; see [20–26] among several others. These schemes are especially attractive in that they do not place any strong restrictions on the flow and are suitable for simulations across a wide range of scales and geometries [27,28]. It was then shown in [29] that, by incorporating the methodology for reformulating the free-surface problem as found in [30], that PVMs could be in effect merged with Dirichlet-to-Neumann Operator (DNO) based methods [31,32] for solving the free-surface problem.

However, in [29], building on work in [33] and explored elsewhere in [34], simulations with up to four vortices were studied, preventing the modeling of more complicated vortex patches underneath free surface waves. Thus, in this paper we present simulations of vortex patches involving several thousands of vortices. To do so, we incorporate into the formulation in [29] many of the techniques for error control and computational efficiency that have been developed in the PVMs community. In particular the use of a Fast-Multipole Method (FMM) [35] and Lagrangian-to Eulerian regridding [21] play critical roles in obtaining our results. Using this machinery in the shallow-water context, we are able to then study the impact of vortex patches on the evolution of free surfaces waves which are approximated by the cnoidal-solutions of the Korteweg–de Vries equation. This is a canonical model for nonlinear, shallow-water free surface waves, and it thus serves as an excellent source for the generation of families of initial conditions for the free-surface state. While used in the context of shallow water and periodic boundary conditions in the present work, the approach to the inclusion of vorticity used in this paper is versatile enough to be applicable to arbitrary depth and arbitrary modeling accuracy, thus providing a distinct complement to the Boussinesq and Green–Naghdi models described above. As we show via extensive numerical simulation, the free surface and vortex patch form a highly complex coupled nonlinear system. In particular, we show that vortex patches may have a significant destabilizing influence on small-amplitude traveling-surface waves. While this effect is predictably augmented by increasing patch strength, there also appears to be a critical patch strength above which the impact of the patch becomes markedly stronger than linear scaling arguments would imply. This instability manifests itself as very strong distortions, and even amplifications, of the surface-wave height, significant changes in the relative energy input from the vortex patch into the surface, and the net displacement and distortion of the patch itself. The impact of the vortex patch is lessened relative to larger amplitude, more nonlinear, traveling free-surface waves moving over the patch (see Fig. 1).

In all, we show lower amplitude surface deformations are potentially unstable with respect to the impact of a vortex patch moving underneath, while larger amplitude, more nonlinear profiles appear relatively robust to the influence of a vortex patch. Such results, and the modeling techniques used, could be pertinent to coastal engineering projects for which underwater vortex patches, generated say by relatively sharp bathymetric features, would then induce larger amplitude nonlinear waves than would be predicted from irrotational modeling, thereby changing safety margins in design. Likewise, when considering near wave-energy extraction device design, a more sophisticated understanding of the impact of vortex patches on surface wave dynamics could allow for more efficient exploitation of the surrounding wave field. In this vein, a future direction of this research will be to assess the impact of vortex patches on the statistical properties of random wave fields, thus providing a deeper appreciation of how overall wave energy responds to underwater eddies. Likewise, there is the question of modeling vorticity in three-dimensional flows. It is shown in [20] that the PVM methods we use

in this paper can be extended to vortex filaments, and the DNO modeling of the free surface is readily extensible to three dimensions. Thus the present results also provide a promising indication of future success in modeling three-dimensional flows.

An overview of the paper is as follows. In Section 2, the model, numerical scheme, and implementation details are presented. Section 3 presents our numerical results, while in Section 4 we summarize our results and speak to future directions of research. Some technical details about the DNO are collected in Appendix.

2. Mathematical model, numerical approach and implementation details

Throughout, we are attempting to describe the simultaneous evolution of a free surface $y = \eta(x, t) + H$, and a compactly supported patch of vorticity $\omega(x, y, t)$ underneath the free surface. Note in particular that we do not make any supposition about any particular coupling between the free surface and the vortex patch such as a traveling wave ansatz [26].

We suppose along the curve $y = 0$ that we have a solid boundary so that the normal velocity is identically zero. In an inviscid, incompressible fluid, we can represent the fluid velocity $\mathbf{u}(x, y, t)$ generated by a vortex patch characterized by vorticity profile $\omega(\mathbf{x}, t)$, $\mathbf{x} = (x, y)$, over the compact domain $\Omega(t)$ via the integral equation

$$\mathbf{u}(\mathbf{x}, t) = \int_{\Omega(t)} \mathbf{K}(\mathbf{x} - \tilde{\mathbf{x}})\omega(\tilde{\mathbf{x}}, t)d\tilde{\mathbf{x}} + \nabla\tilde{\phi}, \ \Delta\tilde{\phi} = 0.$$

where ω is the vorticity, and $\mathbf{K}$ is the standard Biot–Savart kernel given by

$$\mathbf{K}(\mathbf{x}) = \frac{\mathbf{x}^\perp}{2\pi r^2}, \quad \mathbf{x}^\perp = (-y, x), \quad r^2 = x^2 + y^2.$$

The harmonic function $\tilde{\phi}$ is used to address boundary conditions as explained in [36]. A means for discretizing this equation, as summarized in [20], is to approximate the vorticity ω via the expression ω_d which is given by a collection of N point-vortices at positions $\mathbf{x}_j(t)$ via the PVM expansion

$$\omega_d(\tilde{\mathbf{x}}, t) = \sum_{j=1}^{N} \frac{\Gamma_j}{\delta^2} \chi\left(\frac{\tilde{\mathbf{x}} - \mathbf{x}_j(t)}{\delta}\right), \ \mathbf{x}_j(t) = \left(x_j(t), y_j(t)\right), \ \delta > 0, \tag{1}$$

where χ is an appropriately chosen mollifier, see [24], with δ being the 'effective radius', [20], of the mollified point vortices, and Γ_j is the circulation associated with the point vortex at $\mathbf{x}_j(t)$. We can see the connection to circulation by noting that one of the standard requirements for a mollifier $\chi(\tilde{\mathbf{x}}) \geq 0$ is that

$$\int_{\mathbb{R}^2} \chi\left(\tilde{\mathbf{x}}\right) d\tilde{\mathbf{x}} = 1,$$

so that for δ chosen sufficiently small, we have that the mollifier concentrates around a point such that

$$\frac{1}{\delta^2} \int_{C(\mathbf{x}_k, \delta)} \chi\left(\frac{\tilde{\mathbf{x}} - \mathbf{x}_j}{\delta}\right) d\tilde{\mathbf{x}} \sim \delta_{jk},$$

where $C(\mathbf{x}_k, \delta)$ denotes a disc of radius δ centered around the point $\mathbf{x}_k$ and δ_{jk} denotes the Krönecker tensor. Thus we see in the small δ limit that

$$\Gamma_j \sim \int_{C(\mathbf{x}_j, \delta)} \omega_d\left(\tilde{\mathbf{x}}, t\right) d\tilde{\mathbf{x}},$$

as one would expect.

If we start a simulation with the vortices arranged in an equispaced configuration with intervortex separation h, in order to ensure that the above PVM discretization converges to the true dynamics as h is taken to zero, then one must mollify with $\delta > h$. This requirement ensures that the vortices 'overlap' and that particle velocities do not become arbitrarily large due to intervortex proximity, which allows for a rigorous proof of convergence; see [20] for details and the proof.

Using the above discretization, we can reduce the problem of tracking the evolution of the vortex patch to describing the motion of the point vortices via the system of ODE's

$$\frac{d\mathbf{x}_j}{dt} = \sum_{l \neq j}^{N} \Gamma_l \mathbf{K}_\delta\left(\mathbf{x}_j - \mathbf{x}_l\right) + \nabla\tilde{\phi}\left(\mathbf{x}_j, t\right), \ \mathbf{K}_\delta(\mathbf{x}) = \frac{1}{\delta^2} \int_{\mathbb{R}^2} \mathbf{K}(\mathbf{x} - \tilde{\mathbf{x}})\chi\left(\frac{\tilde{\mathbf{x}}}{\delta}\right) d\tilde{\mathbf{x}}.$$

Choosing, as in [24], the mollifier χ to be

$$\chi(r) = 2e^{-r^2} - \frac{1}{2}e^{-r^2/2},$$

introducing periodic boundary conditions in the lateral direction and enforcing the presence of a solid boundary along the curve $y = 0$ through the method of images then modifies the above dynamical system to be

$$i \frac{dz_j^*}{dt} = \frac{1}{2\pi} \left(\sum_{l \neq j}^{N} \Gamma_l \sum_{m=-\infty}^{\infty} \frac{\tilde{\chi}(z_j - z_l - 2Lm; \delta)}{z_j - z_l - 2Lm} - \sum_{l=1}^{N} \Gamma_l \sum_{m=-\infty}^{\infty} \frac{\tilde{\chi}(z_j - z_l^* - 2Lm; \delta)}{z_j - z_l^* - 2Lm} \right) + \partial_y \tilde{\phi} + i \partial_x \tilde{\phi},$$

where $z_j = x_j + i y_j$, the period in x is given by $2L$, and

$$\tilde{\chi}(r; \delta) = \left(1 - e^{-r^2/2\delta^2} \right) \left(1 + 2e^{-r^2/2\delta^2} \right).$$

We evaluate the corresponding sums over the image points $z_j - z_l^*$ so as to keep the zero flow through $y = 0$ condition strictly enforced.

Following the arguments in [29], and again emphasizing the compact support of the vorticity $\omega(x, y, t)$, leads to the coupled nonlinear system

$$\partial_t \eta = -\partial_x \eta \partial_x \tilde{\phi} + \partial_y \tilde{\phi} + P_v,$$

and

$$\partial_t \tilde{\phi} + \frac{1}{2} \left| \nabla \tilde{\phi} \right|^2 + \text{Im} \{Q_v\} \partial_x \tilde{\phi} + \text{Re} \{Q_v\} \partial_y \tilde{\phi} + g\eta = E_v - \frac{1}{2} |Q_v|^2 \tag{2}$$

where we have defined

$$c(\eta, z_j) = \cot \left(\frac{\pi}{2L} \left(\eta + H - z_j \right) \right),$$

so that

$$P_v = \text{Re} \{Q_v\} - \text{Im} \{Q_v\} \partial_x \eta,$$

$$Q_v = \frac{1}{4L} \sum_{j=1}^{N} \Gamma_j \left(c(\eta, z_j) - c(\eta, z_j^*) \right),$$

and

$$E_v = \frac{1}{4L} \sum_{j=1}^{N} \Gamma_j \left(\dot{x}_j \text{Im} \{c(\eta, z_j) - c(\eta, z_j^*)\} + \dot{y}_j \text{Re} \{c(\eta, z_j) + c(\eta, z_j^*)\} \right)$$

We present a brief derivation of Eq. (2) in the Appendix for the sake of completeness. Note, since the mollifier decays exponentially fast, so long as we keep the vortices several multiples of δ away from the free surface, then we incur at most an exponentially small error by ignoring the mollification in the surface terms P_v, Q_v, and E_v.

Defining $q = \tilde{\phi}|_{z=\eta+H}$, standard arguments [29,31] allow for the derivation of series representations to the Dirichlet–Neumann operator (DNO) $G(\eta)$ so that

$$\eta_t = Gq + P_v,$$

and

$$\partial_t q + \frac{1}{2} (\partial_x q)^2 + g\eta - E_v + \frac{1}{2} |Q_v|^2 =$$
$$-\frac{1}{1 + (\partial_x \eta)^2} \left(\left(\left(P_v + \text{Re} \{Q_v\} - \frac{1}{2} (Gq + \partial_x \eta \partial_x q) \right) (Gq + \partial_x \eta \partial_x q) + \text{Im} \{Q_v\} (\partial_x q - \partial_x \eta Gq) \right).$$

Note, in the numerics, it is more convenient and in some ways more physically relevant to solve for the variable $Q = q_x$. We note that the DNO can readily be factored so that $G(\eta)q = \tilde{G}(\eta)Q$, and throughout the remainder of the paper, it is this version of the DNO we work with, though we drop the tilde for the sake of brevity. See the Appendix for a more complete description of details about the DNO.

Thus, the surface-boundary conditions can be recast entirely in terms of surface variables alone. This then leaves the problem of evaluating the derivatives of $\tilde{\phi}$ at the vortex positions. To do this in a way which closes the system of equations in terms of η, q, and z_j, we repeat the arguments in [29], where it was shown that

$$\partial_y \tilde{\phi} + i \partial_x \tilde{\phi} \big|_{z_j} = -\frac{1}{4L} \int_{-L}^{L} \left((c(\eta, z_j) - c^*(\eta, z_j^*)) \partial_x q - i(c(\eta, z_j) + c^*(\eta, z_j^*)) G(\eta)q \right) dx$$

2.1. Implementation details for the fast-multipole method

As can be seen, the presence of the mollifier prevents the closed form evaluation of the sums in m, thereby potentially adding significant overhead in numerical computations, even if fast Fourier transforms are used to evaluate the sums. We note however that

$$\tilde{\chi}(r;\delta) = 1 + \bar{\chi}(r), \ \ \bar{\chi}(r) = \left(1 - 2e^{-r^2/2\delta^2}\right)e^{-r^2/2\delta^2}$$

which tacitly explains the role of mollification, which is to remove singularities in the determination of particle velocities when $|z_j - z_l| \lesssim \delta$. Thus, when we know that $|z_j - z_l| \delta$, we take $\tilde{\chi}(r;\delta) \sim 1$ so that

$$\frac{1}{2\pi}\sum_{m=-\infty}^{\infty} \frac{\tilde{\chi}(z_j - z_l - 2Lm; \delta)}{z_j - z_l - 2Lm} \approx \frac{1}{4L}\cot\left(\frac{\pi}{2L}\left(z_j - z_l\right)\right),$$

where the sum is taken in the principal value sense. In the case that $|z_j - z_l| \lesssim \delta$, we use instead

$$\frac{1}{2\pi}\sum_{m=-\infty}^{\infty} \frac{\tilde{\chi}(z_j - z_l - 2Lm; \delta)}{z_j - z_l - 2Lm} \approx \frac{1}{4L}\cot\left(\frac{\pi}{2L}\left(z_j - z_l\right)\right) + \frac{1}{2\pi}\frac{\bar{\chi}(z_j - z_l; \delta)}{z_j - z_l}.$$

The error incurred in these approximations is only exponentially small.

However, even in the best case scenario, the evaluation of the particle velocities is an $\mathcal{O}(N^2)$ operation, and as we show later, we should anticipate there being large numbers of vortices in order to maintain the accuracy of our simulation. That being said, by employing a multi-level Barnes–Hut algorithm, which is an example of a Fast-Multipole Method (FMM) [35], we can reduce the evaluation of the sums used to compute particle velocities to an $\mathcal{O}(N \log N)$ operation. Further, our use of a FMM for the evaluation of the velocities $\dot{z}_j$ in effect determines all points either far or close to z_j, and thus it naturally selects when to use approximations appropriate for the cases $|z_j - z_l| \leq \delta$ or $|z_j - z_l| > \delta$. The method relies crucially on the rapid convergence of the approximation

$$\cot\left(\tilde{z}_j - \tilde{z}_l\right) \approx \frac{\left(1 - \tan(\tilde{z}_j - c)\tan(c - \tilde{z}_l)\right)}{\tan\left(\tilde{z}_j - c\right)}\sum_{m=0}^{p}(-1)^m\frac{\tan^l\left(c - \tilde{z}_l\right)}{\tan^l\left(\tilde{z}_j - c\right)},$$

where

$$\tilde{z} = \frac{\pi}{2L}z, \ \ \left|\tilde{z}_l - c\right| < \left|\tilde{z}_j - c\right|.$$

Throughout the remainder of the simulations, we choose $p = 10$, which provides the necessary speed-up without sacrificing any significant accuracy in the computation of the point-vortex velocities.

2.2. Shallow-water scalings and the KdV equation

In the present work, the focus is on waves in shallow water. We therefore introduce the scalings

$$\tilde{x} = \frac{x}{\lambda}, \ \tilde{y} = \frac{y}{H}, \ \tilde{t} = \frac{\sqrt{gH}}{\lambda}t, \ \eta = d\tilde{\eta}, \ \tilde{\phi} = \mu\lambda\sqrt{gH}\tilde{\tilde{\phi}}, \ \tilde{\Gamma}_j = \frac{\Gamma_j}{\Gamma},$$

where we define the non-dimensional parameters

$$\mu = \frac{d}{H}, \ \ \gamma = \frac{H}{\lambda}$$

in terms of the characteristic-wave height d, the undisturbed depth H, and a length scale λ which is a characteristic wavelength.

Using the scalings defined above, it can be seen that the vorticity ω should be scaled as

$$\omega = \frac{\mu\sqrt{gH}}{H}\tilde{\omega},$$

so that by using Stokes' theorem, we see the net circulation Γ can be written as

$$\Gamma = \mu\lambda\sqrt{gH}F, \ \ F = \int_{\tilde{\Omega}}\tilde{\omega}d\tilde{A}.$$

Throughout the paper, we make reference to the non-dimensional Froude number F to characterize the strength of the vortex patch.

In the absence of vorticity, taking $\mu \ll 1$ so that the characteristic-wave height d is small compared to the depth H, and $\gamma = \sqrt{\mu}$, so that the depth H is small compared to the characteristic wavelength λ, one can readily show that in the

traveling coordinate $\xi = x - t$ that the long time evolution of the tangential surface velocity $Q = q_x$ and the surface η are found via the Korteweg–de Vries (KdV) equation,

$$2\partial_\tau Q + 3Q\partial_\xi Q + \frac{1}{3}\partial_\xi^3 Q = 0.$$

As is known, the KdV equation has a family of periodic traveling wave solutions of the form

$$Q(x, t) \sim q_0 + 8\tilde{m}^2\kappa^2 \text{cn}^2 \left(\kappa \left(x - \left(1 + \mu\tilde{c}\right)t\right); \tilde{m}\right), \qquad (3)$$

where

$$\tilde{c} = \frac{2}{3}\kappa^2(2\tilde{m}^2 - 1) + \frac{3}{2}q_0,$$

and where $0 \le \tilde{m} < 1$ is the elliptic modulus of the cnoidal function $\text{cn}(\cdot; \tilde{m})$ and where $\mathcal{K}(\tilde{m})$ represents the complete elliptic integral of the first kind. This then implies that the surface profile is to leading order given by $\eta \sim Q$. We then choose initial conditions in our numerical simulations of free surface waves over vortex patches consistent with the traveling wave solutions of the KdV equation. Throughout the remainder of the paper, $q_0 = 0$.

2.3. Implementation details for the lagrangian to eulerian regridding

As noted in [24] and examined in [20] and related papers, a major source of error in PVMs is the implicit grid distortion induced by the Lagrangian flow of the particles $\mathbf{x}_j(t)$. In particular, we can interpret the mollification parameter δ as setting an effective radius of influence for each point $\mathbf{x}_j(t)$. The convergence theory associated with the PVM approximation, see [37], requires that if the particles $\mathbf{x}_j$ start on a uniform mesh with intervortex spacing h, then $h < \delta$, and this 'overlapping' must be maintained for all times of the simulation.

An especially effective means to ensure this was introduced in [21], where at some fixed number of time steps, the set of potentially irregular point positions and circulations, say

$$\left\{\mathbf{x}_j(t), \Gamma_j\right\}_{j=1}^N$$

are mapped onto a new, regularly h-spaced set of positions and corresponding circulations, say

$$\left\{\tilde{\mathbf{x}}_l, \tilde{\Gamma}_l\right\}_{l=1}^{\tilde{N}}.$$

This is done through the choice of a compactly supported interpolation kernel $\Lambda(\cdot)$ so that

$$\tilde{\Gamma}_l = \sum_{j=1}^N \Gamma_j \Lambda\left(\frac{\tilde{x}_l - x_j}{h}\right) \Lambda\left(\frac{\tilde{y}_l - y_j}{h}\right).$$

As in [21], we choose the kernel $\Lambda(x)$ so that

$$\Lambda(u) = \begin{cases} 1 - u^2, & 0 \le |u| < \frac{1}{2} \\ \frac{1}{2}(1 - u)(2 - u), & \frac{1}{2} \le |u| \le \frac{3}{2} \\ 0, & |u| > \frac{3}{2} \end{cases}$$

This choice ensures that the net circulation and the associated first and second moments are preserved after regridding. It should be noted however that regridding in this way generically increases the total particle count so that $\tilde{N} > N$. This is largely due to having to add points $\tilde{\mathbf{x}}_l$ relative to the distorted points $\mathbf{x}_j$ furthest from the interior of the support of $\omega(\mathbf{x}, t)$.

We now model the initial vorticity via the circularly symmetric, compactly supported vorticity profile

$$\omega_0(r) = \begin{cases} \omega_m \left(1 - \frac{r^2}{R_v^2}\right)^3, & r \le R_v \\ 0, & r > R_v \end{cases}$$

Given the circular symmetry of the profile, in the absence of a free surface or solid boundary, we know that $\omega(\mathbf{x}, t) = \omega_0(r)$. Using Eq. (1), we can define a relative error $\mathcal{E}(t)$ via the formula

$$\mathcal{E}(t) = \frac{||\omega_d - \omega||_2}{||\omega||_2} \approx \left(\frac{\sum_{l=1}^{\tilde{N}} \left|\omega_d(\tilde{\mathbf{x}}_l, t) - \omega(\tilde{\mathbf{x}}_l, t)\right|^2}{\sum_{l=1}^{\tilde{N}} \left|\omega(\tilde{\mathbf{x}}_l, t)\right|^2}\right)^{1/2}, \quad ||\omega||_2 = \left(\int_{\Omega(t)} \omega^2(\tilde{\mathbf{x}}, t)d\tilde{\mathbf{x}}\right)^{1/2}.$$

After introducing the shallow-water scalings described above, we choose $\mu = .2$, $\gamma = \sqrt{\mu}$, $\omega_m = 1$, and we run the simulations for $0 \le t \le t_f = 10 = 2/\mu$. Choosing a sampling rate of six time steps with $dt = .05$ and $\delta = 2h$, we produce the following error profiles for $h = .005, .0067,$ and $.01$ in Fig. 2. As can be seen, while the overall error percentages are quite small in all cases, as one would expect, choosing $h = .005$ and then maintaining that throughout the length of the simulation produces the most stable error profile.
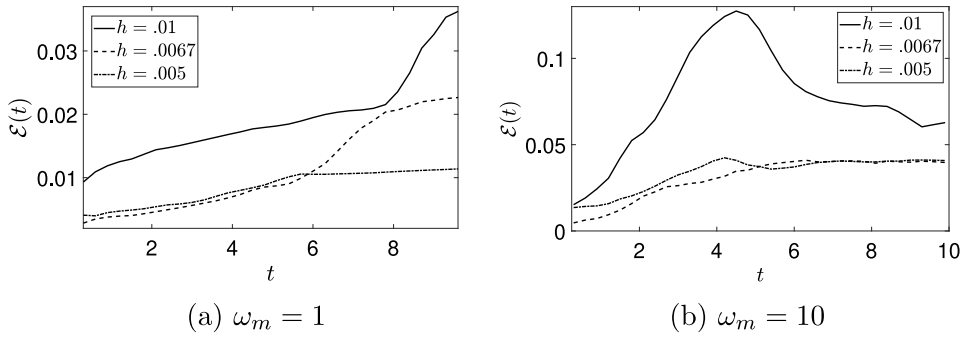
(a) $\omega_m = 1$ (b) $\omega_m = 10$

Fig. 2. Error profiles for $h = .005$, $.0067$, and $.01$ with $\delta = 2h$, $\omega_m = 1$ (a), $\omega_m = 10$ (b), $\delta = 2h$, and regridding is done at every six time steps of the simulation.

Table 1
For varying grid spacings, h, $\delta = 2h$, and with $\omega_m = 10$, the starting particle count N_s and the ending particle count N_f. The increase is a consequence of the regridding procedure, which in this case is done every six time steps of the simulation.

h	N_s	N_f
.005	1252	12,971
.0067	698	8938
.01	308	5911

However, the accuracy of the method must be contrasted against the computational expense incurred by introducing greater number of point-vortices at each regridding event. If we define N_s to be the initial number of point vortices and N_f to be the final number, we get Table 1 for differing values of h over the time interval $0 \leq t \leq t_f$.

Likewise, for the range of vorticity strengths we wish to examine, we see by comparing Figs. 2(a) and (b) that choosing $h = .0067$ and $\delta = 2h$ provides a relatively high-degree of accuracy while keeping the number of point vortices in the simulation at a more manageable level. We therefore stick with this particle spacing throughout the rest of the paper.

The increase in particle count and also position relative to the interior of the vorticity profile also raises the question of newly introduced points running into either the solid boundary at $y = 0$ or the free surface at $y = \mu\eta(x, t) + 1$. As indicated in [29], and supported by the work in [34] among other references, as vortices approach the surface, we should expect overturning or breaking phenomena in the surface. At present, our DNO based numerical method is not able to handle such a case, and therefore we modify the interpolation scheme so that vortices do not propagate past either $z = 0$ or $z = .9$. Thus, while maintaining the accuracy of the PVM, this approach introduces significant overhead in the computation of particle velocities, which again is ameliorated through the use of the FMM.

3. Numerical results

Throughout this section, we take $L = \lambda M$, where M counts the number of characteristic wavelengths included in the computational domain. Correspondingly, we take $M = \mathcal{K}(\tilde{m})/\kappa$, so that the period of the numerical simulation is equal to the period of the cnoidal wave. We note that this does place some limits on the overall elliptic modulus we may pick since as $\tilde{m} \to 1^-$, the solitary wave limit moves the periodic copies of the vortices in the lateral direction off to infinity. This creates a series of source terms in the free boundary equations which decay only quadratically, thereby radically limiting the efficacy of a spectral method for modeling the surface. This is a complication beyond the scope of the present paper, but one that will be explored in future research.

With regards to the details of the simulations, we let $\mu = .2$, $\gamma = \sqrt{\mu}$, which is consistent with the KdV approximation, and $t_f = 2/\mu$, so that nonlinearity has enough time to have a significant impact. Twenty terms are taken in the recursive computation of the DNO, and a total of $K_T = 512$ modes are used for the pseudospectral approximation of the free surface. A Runge–Kutta 4 method with integrating factors, *cf.* [38], is used with a time-step of $\delta t = .05$. We then have for our choice of vortex patch that the parameter F is given by

$$F = \frac{\pi \omega_m R_v^2}{4\gamma}. \tag{4}$$

The radius of the patch, R_v, is chosen so that

$$R_v = \frac{\gamma}{2} \min\{1 - y_c, y_c\} \tag{5}$$

where y_c is the initial vertical displacement of the patch. The initial horizontal displacement is $x_c = 0$. The initial position of the wave is at $x = -M/2$.

With these choices fixed, we note that the unscaled amplitude of the cnoidal wave initial conditions is given by $8(\tilde{m}\kappa)^2$. Throughout our simulations we have chosen κ for a given choice of elliptic modulus $\tilde{m}$ so as to make this unscaled amplitude as close to unity as possible while still maintaining convergent numerical simulations. The issue for convergence in the DNO is a complicated one [32,39], though the issue can be mollified by reducing the size of μ. This of course adds further choices in parameters, which are already numerous as is. While in this paper we have chosen to stick with the DNO approach due to its relative ease of implementation, there are similar but more stable approaches such as the Transformed Field Expansion [40] which should be adaptable to this problem. Exploring this issue is a subject of future research.

In each of the following plots, we look at both the evolution of the vortex patch, and a comparison of the evolution of the free surface from the same initial conditions. Solid lines correspond to results in which $F \neq 0$ while dashed lines correspond to the zero vorticity, or $F = 0$, case. To better understand the impact of vortex patches on the cnoidal wave profiles examined in this work, we also provide a more quantitative measure of the impact of the vortex patch. This is done by plotting a relative comparison of the total energy in the surface, where the total energy in the surface in the shallow-water coordinates is given by

$$E(t; F) = \frac{1}{2} \int_{-M}^{M} \left(q G(\eta) Q + \eta^2 \right) dx, \ \ Q = q_x,$$

where we have emphasized the role of the patch through the implicit inclusion of the parameter F. In the absence of a vortex patch, i.e. $F = 0$, $E(t; 0)$ is a conserved quantity of the flow since it serves as the Hamiltonian of the dynamical system describing the surface dynamics [41]. Thus, in the following figures, we plot the relative difference in energy $\delta E(t; F)$ where

$$\delta E(t; F) = \frac{E(t; F) - E(t; 0)}{E(t; 0)}.$$

We likewise compute the mean relative-energy input δE_m where

$$\delta E_m = \frac{1}{t_f} \int_0^{t_f} \delta E(t; F) dt = \frac{1}{E(t; 0)} \left(\frac{1}{t_f} \int_0^{t_f} E(t; F) dt - E(t; 0) \right),$$

where in the last equality we have used the fact that $E(t; 0) = E(0; 0)$ since it is a conserved quantity of the flow. Finally, we also track the horizontal center-of mass of the vortex patch, say $x_c(t)$, defined by the formula

$$x_c(t) = \frac{\int_{\tilde{\Omega}(t)} x \tilde{\omega}(x, y, t) d\tilde{A}}{\int_{\tilde{\Omega}(t)} \tilde{\omega}(x, y, t) d\tilde{A}},$$

thereby allowing us to better understand the impact of the traveling wave on the motion of the patch.

Contemplating the impact of the patch on the surface, we note that the speed of waves at the surface to leading order is given by $c_w = 1$ in our non-dimensionalized coordinates. As is known from the literature on bathymetric variations in shallow-water models, see [42] and references therein, when underwater objects, which necessarily induce pressure fluctuations at the surface, propagate at a speed near c_w, then resonance occurs manifesting itself as the generation of nonlinear waves at the surface. It is therefore interesting to estimate what the speed of a given patch is and thus how near or far its speed is with regards to c_w. To estimate the patch speed, if we placed a point vortex y_c in a domain with a flat surface, then the vortex would propagate initially with the horizontal velocity

$$u_p = \frac{\mu F}{4\gamma} \cot(\pi y_c).$$

While later surface disturbances will modify this speed, it is nevertheless a good leading estimate for the overall patch speed. We see then that when $u_p = c_w = 1$, the critical Froude value F_w is given by

$$F_w = \frac{4\gamma}{\mu} \tan(\pi y_c).$$

Throughout the simulations that follow, we choose $\mu = .2$ and $\gamma = \sqrt{\mu}$. In this case then, one has that $F_w \sim 1$ for $y_c \sim .035$, or $y_c \sim .965$ so that waves propagate in the other direction. Thus critical phenomena at most depths correspond to relatively large Froude numbers of the patch. While we have tried exploring phenomena related to critical Froude numbers, such strong patches push our numerical scheme into relatively unstable regimes demanding more care in how we model the surface, where breaking phenomena should be expected, and in terms of time-step and sampling restrictions on the motion of the patch, which is to be expected to exhibit strong self-interactions. Addressing these issues is extremely interesting, but is beyond the scope of the current paper.

Likewise, throughout the following simulations, we take $y_c = .35$. This proved to be a stable enough choice so that we could examine Froude numbers up to $F = .5$ while still maintaining reasonable run times, accuracy, and stability in the numerics. We point out that while some of our issues pertain to the complexity of simulating the patch dynamics,
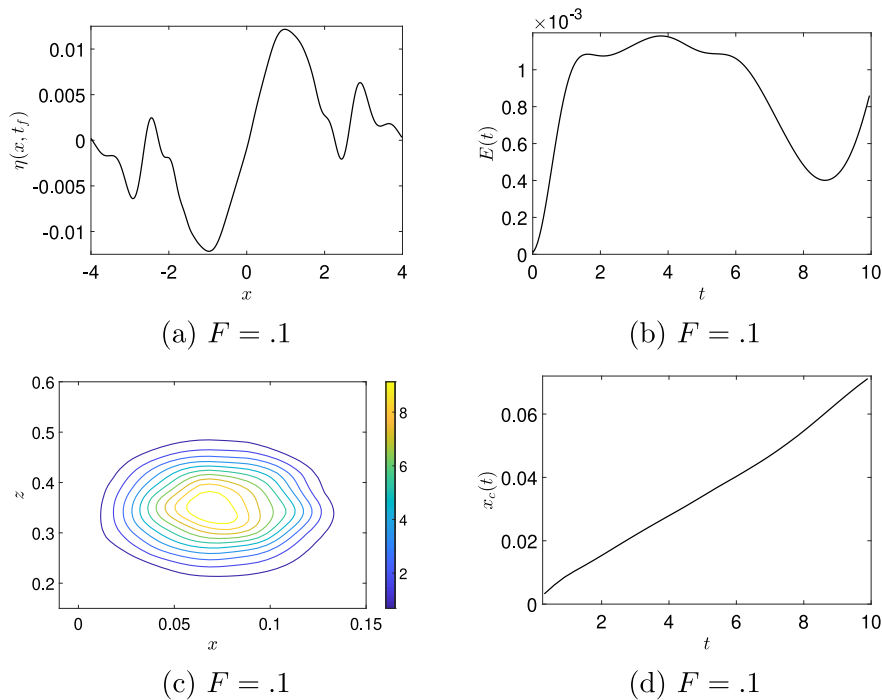
(a) $F = .1$

(b) $F = .1$

(c) $F = .1$

(d) $F = .1$

Fig. 3. Profile (a), energy input (b), final vortex patch position and shape (c), and motion of the patch's horizontal center-of mass (d) for an initially still surface. Here $F = .1$, $\mu = .2$, $\gamma = \sqrt{\mu}$, and $t_f = 2/\mu$.

much of the constraints in our numerics have to do with the modeling of the free surface. To explore this, motivated by the results in [33] and later in [34], our method of course works for a single point vortex; see [29] for details and a more extensive bibliography on numerical studies of free waves over point vortices. Thus, we have compared our patch results to ones with only a single-point vortex of equal Froude number at the same starting depth.

In all cases, the surface dynamics are essentially identical to those involving a patch, thereby providing a check on our overall numerical method. However, our numerical experiments with even a single vortex show that if we take $F = 1$, by making $y_c > .15$, singular phenomena appears in the surface, mostly likely reflecting overturning or breaking phenomena. Thus, by drastically reducing the Froude number, we can examine point vortices at higher positions, even having them approach the surface; again see [29]. However, to simulate patches at higher vertical positions which still have order one Froude numbers clearly requires a more sophisticated approach than using the relatively straightforward DNO approach. This again is a subject of future research.

3.1. Initially quiescent free surface

To develop intuition and establish base line metrics with which to compare later results, we study an initially quiescent surface so that $\eta(x, 0) = 0$, and $\tilde{\phi}(x, 0)$ is chosen so as to make the initial surface velocity identically zero. We take the domain to be $-4 \leq x \leq 4$, which is comparable to the later domain sizes. Taking $F = .1$, representing the high end of the cases we examine later in the paper, we then generate Fig. 3.

As seen, the patch induces significant deformations of the surface, though they are relatively small. Interestingly, the energy input rapidly saturates and then decreases while the patch slowly moves from left to right. The fact that the displacement of the horizontal center-of mass of the patch only reaches to about $x = .07$ for $t_f = 2/\mu = 10$ shows that the impact of the image points due to the solid boundary at $y = 0$ is relatively weak.

3.2. Elliptic modulus $\tilde{m} = .3$

Taking $\tilde{m} = .3$ and $\kappa = .5$ corresponds to $M \approx 3.3$, and taking $K_T = 512$ gives $\delta x = .013$. The unscaled amplitude of the cnoidal initial conditions is given by $8(\tilde{m}\kappa)^2 \approx .18$. From both the pointwise comparisons in Fig. 4 and the relative energy inputs in Fig. 4, we see that stronger vorticity corresponds to greater deformation of the surface wave relative to the undisturbed case, and comparing across Figs. 6 and 8, we see that the vortex patch has the strongest impact on the least nonlinear waves.
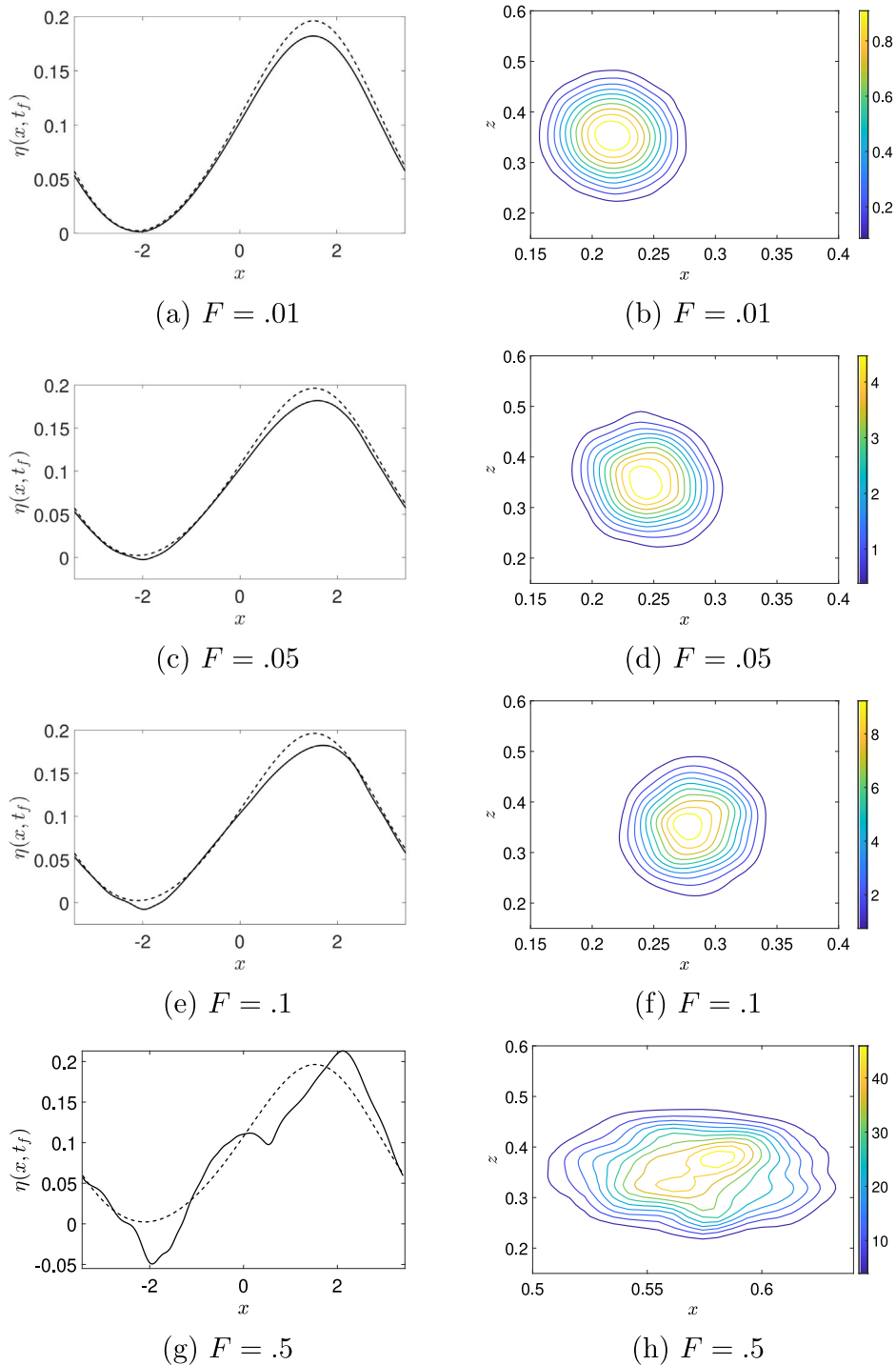
Fig. 4. Comparisons of a cnoidal wave over a vortex patch(-) to a cnoidal wave over an irrotational fluid (- -) at $t = t_f$ are shown on the left for various values of the Froude number F, while the final position, shape, and strength of the vortex patch is shown on the right. Here $\mu = .2$, $\gamma = \sqrt{\mu}$, $t_f = 2/\mu$, $\tilde{m} = .3$, $\kappa = .5$.

As seen though in Fig. 4, a ten-fold increase in F from $F = .01$ to $F = .1$ induces a relatively linear change in the response of the vortex patch and free surface system. The modification of the surface is relatively mild; see Figs. 4(a), (c), and (e), with slight differences seen in the vortex patch position and shape; see Figs. 4(b), (d), and (f). Likewise, the

Table 2
Mean relative-energy input
for $\tilde{m} = .3$ and $\kappa = .5$.

F	δE_m
.01	-1×10^{-3}
.05	-3.6×10^{-3}
.1	-3.7×10^{-3}
.5	1.3×10^{-1}

Table 3
Mean relative-energy input
for $\tilde{m} = .6$ and $\kappa = .43$.

F	δE_m
.01	-1.7×10^{-4}
.05	-7×10^{-4}
.1	-1.1×10^{-3}
.5	8.8×10^{-3}

difference in the relative energy inputs plotted in Figs. 5(a), (c), and (e) show changes following a linear increase in the Froude number. Where one can see a nonlinear coupling between the surface and the patch is in the mean-energy input compiled in Table 2. Clearly increasing the Froude number from $F = .01$ to $F = .1$ does not induce a linear change in δE_m. We also see that $\delta E_m < 0$ in these cases, reflecting a loss of energy from the surface to the patch.

We also see the impact of this energy transfer from the surface wave to the vortex patch in the patch displacement measured by the horizontal center-of-mass $x_c(t)$ plotted in Figs. 5(b), (d), (f) and (h). As can be seen, the displacement is far greater in this case relative to the quiescent surface example shown in Fig. 3. Indeed, examining Fig. 5, we see that the center-of-mass of the patch has been displaced on average about .25 non-dimensional units relative to its starting position, which is significantly further than in the quiescent surface case examined above. The periods of acceleration seen by examining the center-of-mass positions in Figs. 5(b), (d), (f) and (h) correspond to the wave crest moving over the patch. The difference in final displacement of the patch increases with increasing Froude number, which is to be expected due to the influence of the solid boundary and the corresponding image points (see the left-hand side of Fig. 5). However, it is clear that the solid boundary as a means of patch transport has minimal influence.

However, when the Froude number is increased to $F = .5$, a threshold representing the nonlinear coupling of the patch to the surface has been crossed. Aside from the markedly stronger deformations of both the surface, see Fig. 4(g) in which wave amplitude is amplified as opposed to attenuated, and the patch, see Fig. 4(h), we see the relative mean energy input is positive and two orders of magnitude larger than for $F = .1$; see Table 2. Likewise, the time dynamics of the relative energy input in Fig. 5(g) is, as expected, far more biased towards the patch putting energy into the surface. However, we see from Fig. 5 that the vortex patch also travels two to three times further than in the lower Froude number cases examined above.

3.3. Elliptic modulus $\tilde{m} = .6$

Taking $\tilde{m} = .6$, we find that $\kappa = .43$, and this corresponds to $M \approx 4.4$. Taking $K_T = 512$, this gives $\delta x = .0172$. The unscaled amplitude of the cnoidal initial conditions is given by $8(\tilde{m}\kappa)^2 \approx .53$. As seen in Fig. 6, we see that the larger elliptic modulus and larger amplitude makes the surface wave less responsive to the impact of vorticity. Nevertheless, the patch consistently lowers maximum amplitudes, and when its strength is large enough, induces significant oscillations in the surface profile.

However, in contrast to the $\tilde{m} = .3$ case above, we see that the response of the relative energy input $\delta E(t; F)$ is far more linear in nature, with peaks and troughs being enhanced about equally with rising values of F until a threshold is crossed which leads to a net positive input of energy into the surface for $F = .5$. The mean relative-energy inputs δE_m listed in Table 3 bear this more linear response out, though again the values are always negative implying again that energy is lost from the wave and put into the patch.

In Figs. 7(b), (d), (f) and (h) we see that a relatively larger amplitude, wider surface wave is able to displace the patch significantly further, with mean displacement about .525 non-dimensional units for $F \leq .1$. Again, while the impact of the solid wall along the bottom allows for greater displacement due to larger Froude number, this is nowhere near as significant as the impact of the wave on the patch. We see in Fig. 7(h) for $F = .5$ that the patch displacement is markedly further than for lower Froude numbers, again showing the implicit threshold for the Froude number after which the patch has more impact on the surface, and we observer far greater deformations of both.
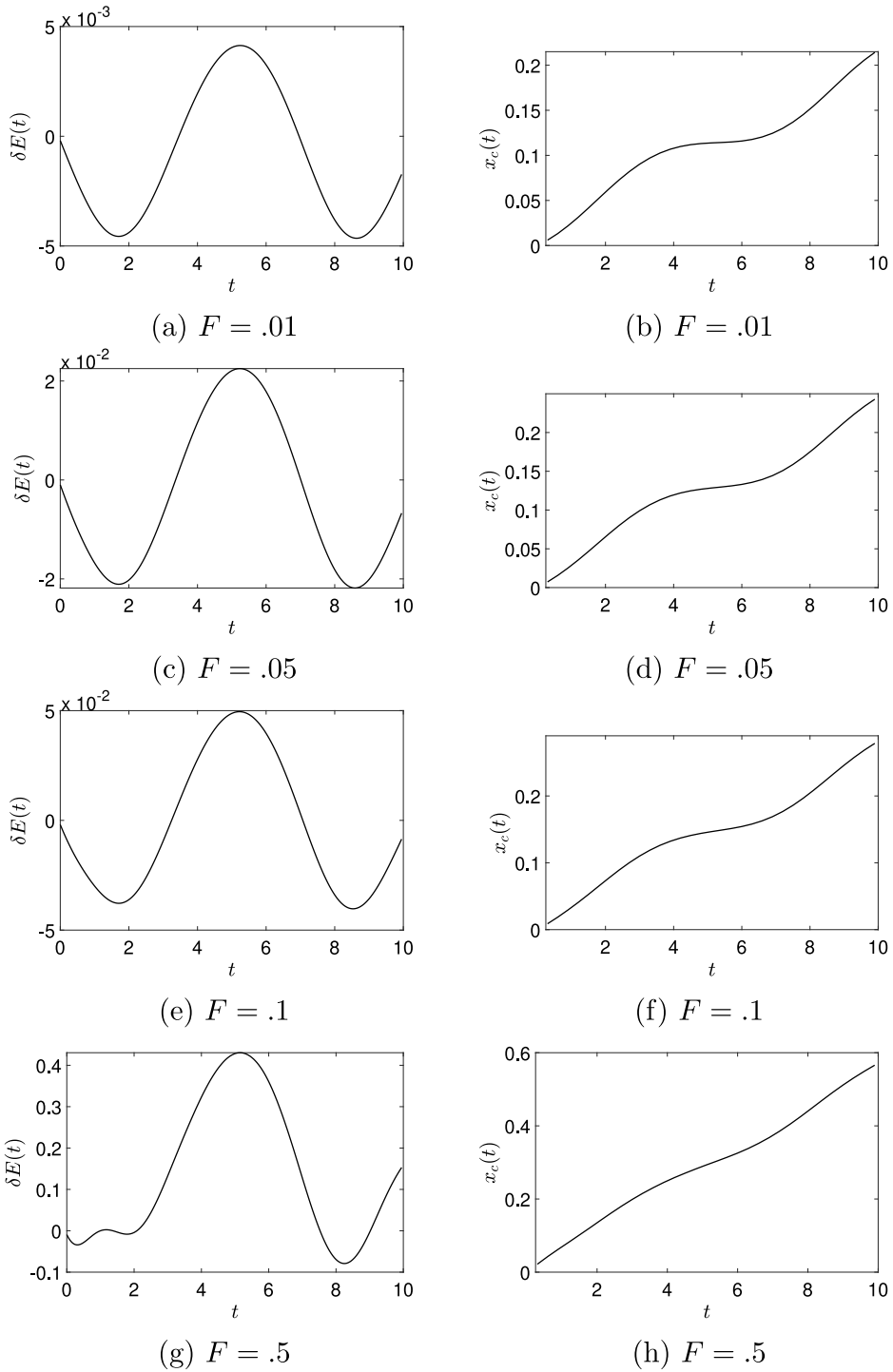
Fig. 5. The relative energy input into the free surface is shown on the left, while the motion of the horizontal center of mass $x_c(t)$ is shown on the right for $\tilde{m} = .3$ and $\kappa = .5$.

3.4. Elliptic modulus $\tilde{m} = .9$

Taking $\tilde{m} = .9$, we find that $\kappa = .35$, this corresponds to $M \approx 7.4$. Taking $K_T = 512$, this gives $\delta x = .029$. The unscaled amplitude of the cnoidal initial conditions is given by $8(\tilde{m}\kappa)^2 \approx .8$. Thus, somewhat surprisingly, we could use

(a) $F = .01$

(b) $F = .01$

(c) $F = .05$

(d) $F = .05$

(e) $F = .1$

(f) $F = .1$

(g) $F = .5$

(h) $F = .5$
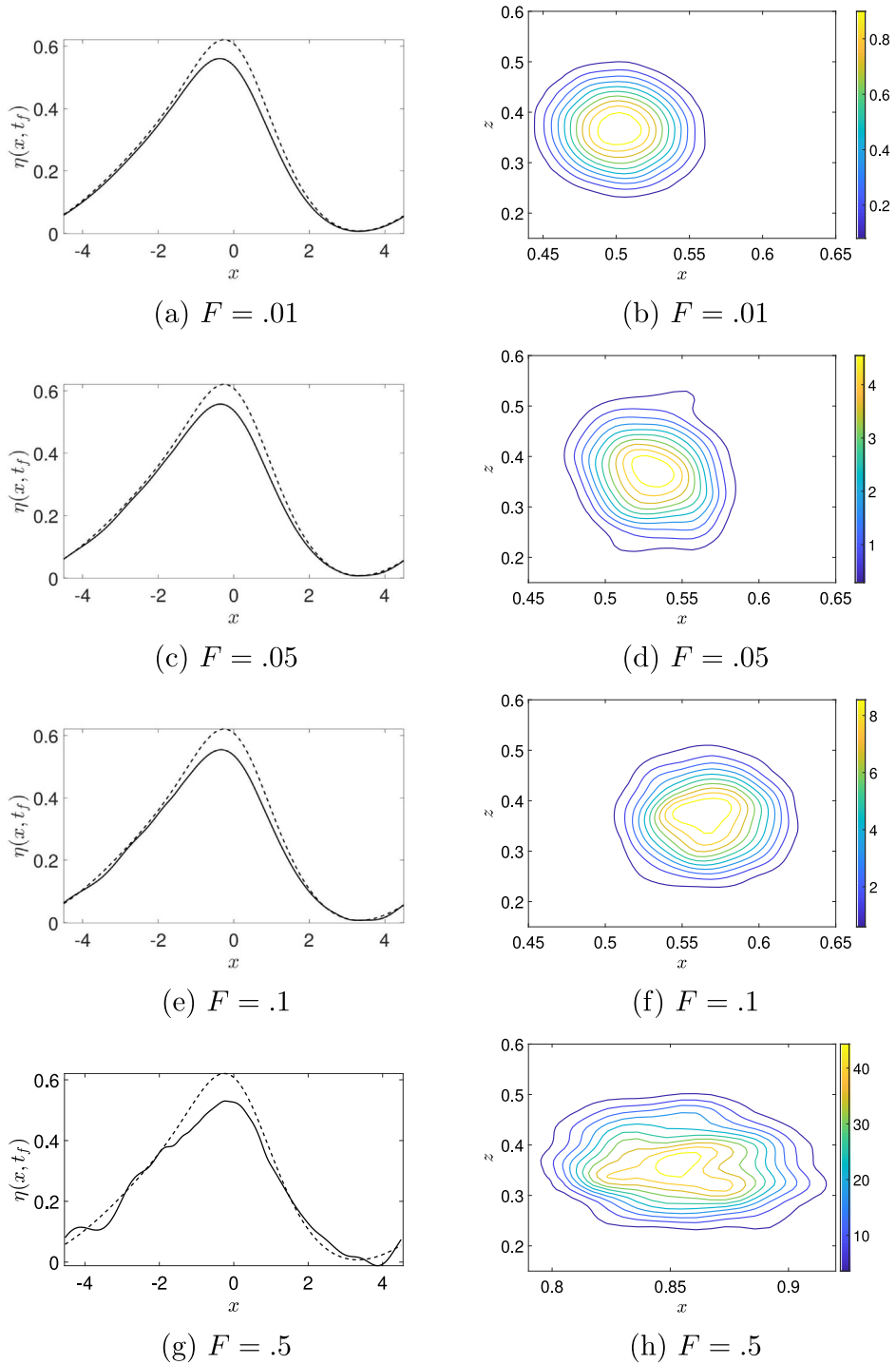
Fig. 6. Comparisons of a cnoidal wave over a vortex patch(-) to a cnoidal wave over an irrotational fluid (- -) at $t = t_f$ are shown on the left for various values of the Froude number F, while the final position, shape, and strength of the vortex patch is shown on the right. Here $\mu = .2$, $\gamma = \sqrt{\mu}$, $t_f = 2/\mu$, $\tilde{m} = .6$, $\kappa = .43$.

the largest amplitude wave when the initial condition was closest to that of a solitary wave profile. Likewise, aside from causing a slight broadening and thus decrease in maximum amplitude of the near solitary wave, vorticity has the least relative impact on the wave. Thus, if we treat the $\tilde{m} = .9$ as the 'most' nonlinear of the three cases examined, since this
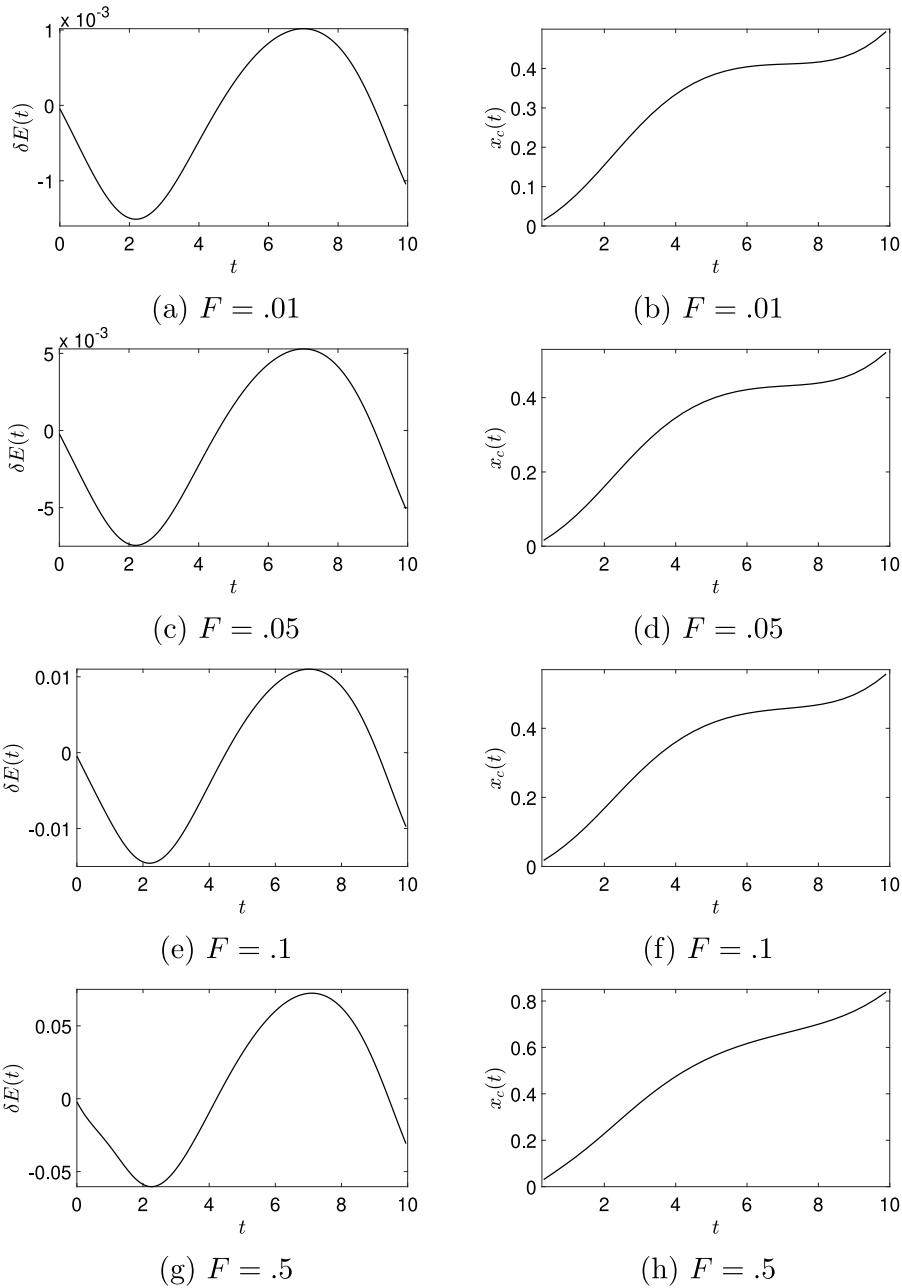
Fig. 7. The relative energy input into the free surface is shown on the left, while the motion of the horizontal center of mass $x_c(t)$ is shown on the right for $\tilde{m} = .6$ and $\kappa = .43$.

corresponds to the case closest to that of a nonlinear solitary wave, we see vorticity has the least overall impact on the most nonlinear of waves.

This is especially seen by the weak response of $\delta E(t; F)$ plotted in Fig. 8. We also get the clearest correlation between the loss in amplitude seen in Fig. 8 and the relative energy input, which is largely negative though stretched out over a longer time scale than in comparison to the energy dynamics seen above. Looking at the relative energy-input in Table 4, we see the most linear response to increasing Froude number compared to the more linear waves examine above, even for $F = .5$ which in the previous surface wave cases studied above corresponded to dynamics being far more nonlinear. However, for $F = .5$, we do see in Fig. 8(h) that significant a impact of the waves on the vortex patch has occurred. Moreover, the net patch displacement is markedly larger than the linear increase in F should account for, so there is still an aspect of threshold behavior for when $\tilde{m} = .9$.
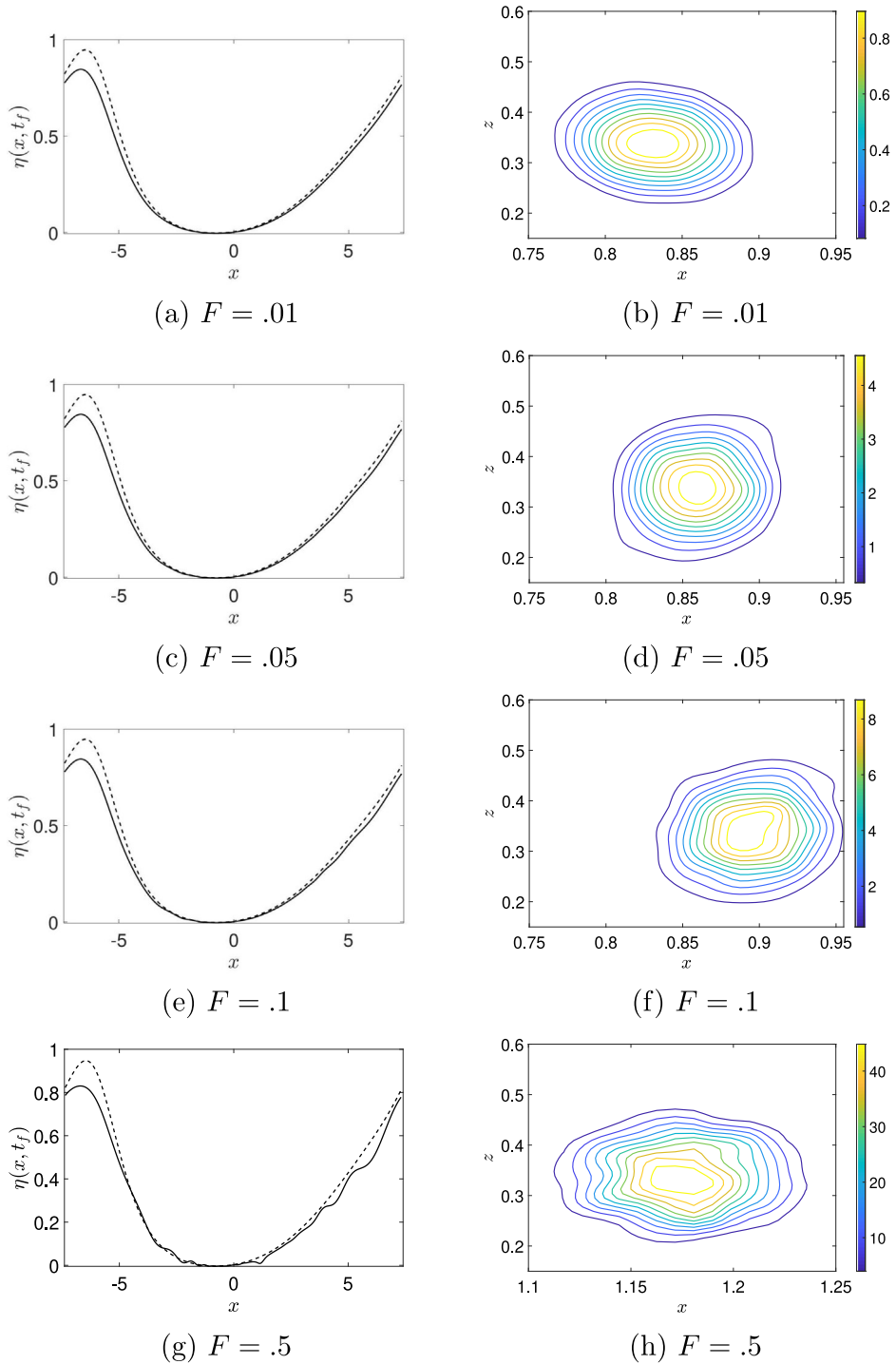
Fig. 8. Comparisons of a cnoidal wave over a vortex patch(-) to a cnoidal wave over an irrotational fluid (- -) at $t = t_f$ are shown on the left for various values of the Froude number F, while the final position, shape, and strength of the vortex patch is shown on the right. Here $\mu = .2$, $\gamma = \sqrt{\mu}$, $t_f = 2/\mu$, $\tilde{m} = .9$, $\kappa = .35$.

We also see in Fig. 9 that the center of the patch is displaced at the greatest distance relative to its starting position, showing the strong effect that relatively large amplitude, wide nonlinear waves have on the patch. Note, across the values of $\tilde{m}$ and κ used throughout this section, the KdV cnoidal wave speed $\tilde{c}$ varies from $\tilde{c} = -.1367$ for $\tilde{m} = .3$, $\kappa = .5$, to $\tilde{c} = .0506$ for $\tilde{m} = .9$, $\kappa = .35$. Thus, working in the fast coordinate and taking $\mu = .2$, we have a net wave speed of

Table 4
Mean relative-energy input for $\tilde{m} = .9$ and $\kappa = .35$.

F	δE_m
.01	-3.87×10^{-4}
.05	-1.9×10^{-3}
.1	-3.7×10^{-3}
.5	-1.5×10^{-2}

.9727 on the low side to 1.0101 on the high side. Therefore, there does not appear to be a significant enough variation in wave speed to explain the differences in the relative displacements of the vortex patches across all the cases studied in this paper. Thus, it appears that wave amplitude and width are the better determining factors for patch displacement, though the full nature of how these parameters interact with the Froude number is a subject of future study.

4. Conclusion

Based on previous work in [29], it has been shown that the reformulation of the free-surface problem due to [30] can be coupled with existing point-vortex methods in order to simulate the simultaneous development of a free surface interacting with a vortex patch in an incompressible inviscid fluid. The numerical discretization is based on Dirichlet-to-Neumann operator methods such as detailed in [31,32] coupled with an approximation of the vortex patch by hundreds or thousands of point vortices each carrying a small amount of the total circulation.

The main focus in the present paper has been on detailed numerical simulations of a vortex patch evolving under certain types of shallow-water free-surface waves. Via our simulations, we have shown how these vortex patches induce non-trivial deformations of propagating nonlinear waves coming from the shallow-water limit. One finding which deserves note is that the deformations of the free surface are especially significant when the waves are of low amplitude, near linear modes.

Our simulations allow for greater quantitative insight by tracking the relative energy transfer and center-of-mass motion of the vortex patches, the dynamics and features of which are shown to correlate strongly with the presence or absence of significant deformations in the surface wave. One finding which is less surprising but nevertheless interesting is that large Froude numbers lead to rapid decomposition of the otherwise coherent vortex patch.

Possible non-trivial extensions of the present work include the use of transformed field expansions [40] in order to further stabilize the numerical computations, and modification of our approach in order to enable the treatment of vortex patches interacting with waves in deep water. Another important future direction will be understanding to what extent the presence of vortex patches influences the properties of breaking waves. The diagnostic parameters used for example in [43] can be readily implemented in our method.

Acknowledgments

Appendix

A.1. Details about the derivation of Bernoulli's equation

To derive Eq. (2), we make use of a result in [44], which shows, making no assumption on the behavior of the vorticity, that the following conservation law holds at the free surface $y = \eta(x, t)$

$$\partial_t \mathcal{C} + \partial_x \left(u\mathcal{C} + g\eta - \frac{1}{2} |\mathbf{u}|^2 \right) = 0, \ \mathcal{C} = \mathbf{u} \cdot (1, \partial_x \eta), \ \mathbf{u} = (u, w).$$

Assuming the compactly supported vortex patch $\omega(x, y, t)$ does not intersect the free surface, we can then write the fluid velocity $\mathbf{u} = \nabla \bar{\phi}$, where

$$\bar{\phi} = \phi_v + \tilde{\phi}, \ \phi_v(\mathbf{x}, t) = \int_\Omega \tilde{K}(\mathbf{x}, \tilde{\mathbf{x}}) \omega(\tilde{\mathbf{x}}, t) d\tilde{\mathbf{x}}$$
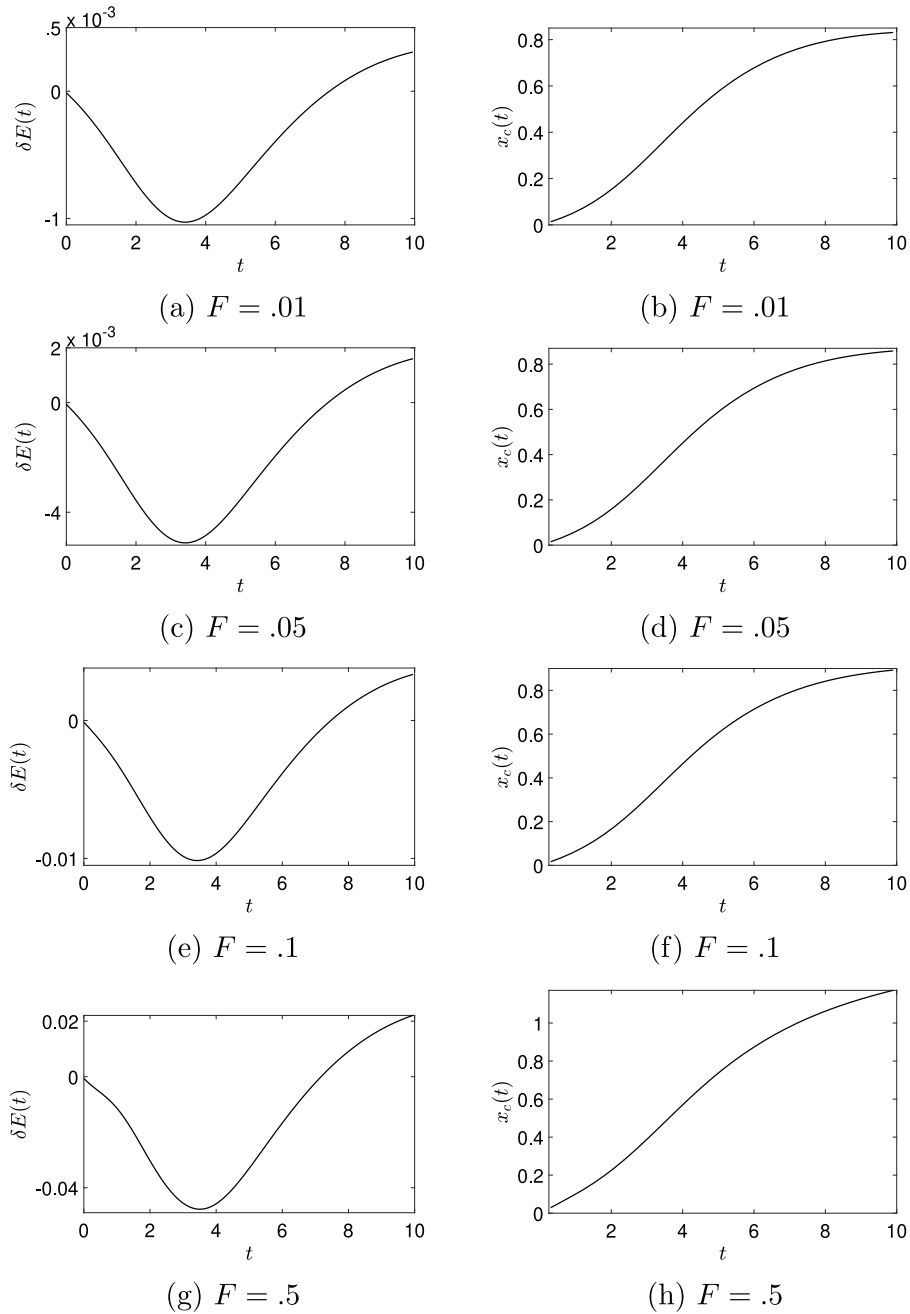
Fig. 9. The relative energy input into the free surface is shown on the left, while the motion of the horizontal center of mass $x_c(t)$ is shown on the right for $\tilde{m} = .9$ and $\kappa = .35$.

where $\tilde{K}$ is the associated harmonic conjugate to the stream function which defines the Biot–Savart kernels and the periodic extensions thereof. We readily see then that

$$\mathcal{C} = \partial_x \bar{\phi}\big|_{y=\eta}.$$

Integrating the conservation law in x and setting the associated integration constant to zero then gives us the Bernoulli equation for $\bar{\phi}$ at $y = \eta$ i.e.

$$\partial_t \bar{\phi} + \frac{1}{2}\left|\nabla\bar{\phi}\right|^2 + g\eta = 0, \ y = \eta(x, t).$$

Using the PVM to discretize ω and ignoring the mollification then gives Eq. (2), though see [29] for more details.

A.2. Details about the DNO

We here provide details about the Dirichlet-to-Neumann Operator (DNO) for the sake of completeness; see [31,32] for greater details. The DNO $G(\eta)$ in the shallow-water scalings used throughout the body of the paper is found via expanding in powers of η so that the kinematic condition becomes

$$\eta_t - \frac{1}{\gamma}P_v(x, 1 + \mu\eta, t) = \left(G_0 + \mu G_1 + \mu^2 G_2 + \cdots\right)Q.$$

Defining the Fourier transform of a periodic function $f(x)$ to be $\hat{f}$, so that

$$\hat{f}(k) = \frac{1}{2M}\int_{-M}^{M} f(x)e^{-i\pi kx}dx, \ \ k \in \mathbb{Z},$$

we define, for a linear operator L, its associated symbol $\hat{L}(k)$ by way of the formula

$$\hat{L}(k)\hat{f}(k) = \frac{1}{2M}\int_{-M}^{M} Lf(x)e^{-i\pi kx/M}dx.$$

We then get

$$\hat{G}_0(k) = -\frac{i}{\gamma}\tanh(\pi\gamma k),$$

and, for $m \geq 1$,

$$G_m Q = -\sum_{j=1}^{\lfloor m/2 \rfloor} \frac{1}{(2j)!}D_\gamma^{2j}\left(\eta^{2j}G_{m-2j}Q\right)$$

$$- \gamma^2\partial_x G_0 ......\sum_{j=0}^{\lfloor (m-1)/2 \rfloor} \frac{D_\gamma^{2j}}{(2j+1)!}\left(\eta^{2j+1}G_{m-2j-1}Q\right) - \frac{1}{m!}L_m\partial_x D_\gamma^{m-1}\left(\eta^m Q\right),$$

where

$$\hat{D}_\gamma = \pi\gamma k,$$

and

$$\hat{L}_m = \begin{cases} 1, & m \text{ is odd}, \\ i\gamma\hat{G}_0(k), & m \text{ is even}. \end{cases}$$

This recursive formula is readily computable, and for the shallow-water scalings we pick, achieving machine-precision is relatively straightforward.

References

[1] H. Lamb, Hydrodynamics, Dover, New York, N.Y., 1945.
[2] P.K. Kundu, I.M. Cohen, Fluid Mechanics, fourth ed., Elsevier, New York, N.Y, 2008.
[3] L.H. Holthuijsen, Waves in Oceanic and Coastal Waters, Cambridge University Press, Cambridge, 2007.
[4] D.I. Pullin, R. Grimshaw, Nonlinear interfacial progressive waves near a boundary in a Boussinesq fluid, Phys. Fluid 26 (1983) 897.
[5] J.A. Simmen, P.G. Saffman, Steady deep-water waves on a linear shear current, Stud. Appl. Math. 75 (1985) 35–57.
[6] A.F. Teles da Silva, D.H. Peregrine, Steep, steady surface waves on wter of finite depth with constant vorticity, J. Fluid Mech. 195 (1988) 281–302.
[7] A.D.D. Craik, The generalized Lagrangian-mean equations and hydrodynamic stability, J. Fluid Mech. 125 (1982) 27–35.
[8] A.D.D. Craik, Wave-induced longitudinal-vortex instability in shear flows, J. Fluid Mech. 125 (1982) 37–52.
[9] P. Drazin, W. Reid, Hydrodynamic Stability, Cambridge University Press, Cambridge, 1981.
[10] O. Nwogu, Interaction of finite-amplitude waves with vertically sheared current fields, J. Fluid Mech. 627 (2009) 179–213.
[11] K.A. Chang, T.J. Hsu, P.L.F. Liu, Vortex generation and evolution in water waves propagating over a submerged rectangular obstacle. Part I: Solitary waves, Coast. Eng. 44 (2001) 13–36.
[12] K.A. Chang, T.J. Hsu, P.L.F. Liu, Vortex generation and evolution in water waves propagating over a submerged rectangular obstacle. Part II: cnoidal waves, Coast. Eng. 52 (2005) 257–283.
[13] C. Lin, T.C. Ho, S.C. Chang, S.C. Hsieh, K.A. Chang, Vortex shedding induced by a solitary wave propagating over a submerged vertical plate, Int. J. Heat Fluid Flow 26 (2005) 894–904.
[14] O. Nwogu, Alternative form of Boussinesq equations for nearshore wave propagation, J. Waterw. Port Coast. Eng. 119 (1993) 618–638.
[15] Q. Chen, J.T. Kirby, R.A. Dalrymple, F. Shi, E.B. Thornton, Boussinesq modeling of longshore currents, J. Geophys. Res. 108 (2003) 26–43.
[16] Y. Zhang, A.B. Kennedy, N. Panda, C. Dawson, J.J. Westerink, Boussinesq-Green-Naghdi rotational water wave theory, Coast. Eng. 73 (2013) 13–27.

[17] A. Castro, D. Lannes, Well-posedness and shallow-water stability for a new Hamiltonian formulation of the water waves equations with vorticity, Indiana Univ. Math. J. 64 (2014) 1169–1270.
[18] A. Castro, D. Lannes, Fully nonlinear long-wave models in the presence of vorticity, J. Fluid Mech. 759 (2014) 642–675.
[19] D. Lannes, F. Marche, Nonlinear wave–current interactions in shallow water, Stud. Appl. Math. 136 (2016) 382–423.
[20] G.H. Cottet, P.D. Koumoutsakos, Vortex Methods: Theory and Practice, Cambridge University Press, Cambridge, 2000.
[21] P. Koumoutsakos, A. Leonard, High-resolution simulations of the flow around an impulsively started cylinder using vortex methods, J. Fluid Mech. 296 (1995) 1–38.
[22] P. Koumoutsakos, Invisicd axisymmetrization of an elliptical vortex, J. Comput. Phys. 138 (1997) 821–857.
[23] R. Krasny, Vortex sheet computations: Roll-up, waves, separation, Lect. Appl. Math. 28 (1991) 385–402.
[24] J.T. Beale, A. Majda, High order accurate vortex methods with explicit velocity kernels, J. Comput. Phys. 58 (1985) 188–208.
[25] A.J. Majda, A.L. Bertozzi, Vorticity and Incompressible Flow, Cambridge University Press, Cambridge, 2002.
[26] J. Shatah, S. Walsh, C. Zeng, Travelling water waves with compactly supported vorticity, Nonlinearity 26 (2013) 1529–1564.
[27] P. Koumoutsakos, Multiscale flow simulations using particles, Ann. Rev. Fluid Mech. 37 (2005) 457–487.
[28] W.M. van Rees, A. Leonard, D.I. Pullin, P. Koumoutsakos, A comparison of vortex and pseudo-spectral methods for the simulation of periodic vorical flows at high Reynolds numbers, J. Comput. Phys. 230 (2011) 2794–2805.
[29] C.W. Curtis, H. Kalisch, Vortex dynamics in free-surface flows, Phys. Fluids 29 (2017) 032101.
[30] M.J. Ablowitz, A.S. Fokas, Z.H. Musslimani, On a new non-local formulation of water waves, J. Fluid Mech. 562 (2006) 313–343.
[31] W. Craig, C. Sulem, Numerical simulation of gravity waves, J. Comput. Phys. 108 (1993) 73–83.
[32] P. Guyenne, D.P. Nicholls, A high-order spectral method for nonlinear water waves over moving bottom topography, SIAM J. Sci. Comput. 30 (2007) 81–101.
[33] P.A. Tyvand, On the interaction between a strong vortex pair and a free surface, J. Fluid Mech. 225 (1991) 673–686.
[34] A. Doak, J.M. Vanden-Broeck, Solitary gravity waves and free surface flows past a point vortex, IMA J. Appl. Math. 82 (2017) 821–835.
[35] L. Greengard, V. Rokhlin, A fast algorithm for particle simulations, J. Comput. Phys. 73 (1987) 325–348.
[36] P.G. Saffman, Vortex Dynamics, Cambridge University Press, Cambridge, 1992.
[37] G.H. Cottet, A new approach for the analysis of vortex methods in 2 and 3 dimensions, Ann. Inst. Henri Poincaré 5 (1988) 227–285.
[38] L.N. Trefethen, Spectral Methods in Matlab, SIAM, Philadelphia, PA, 2000.
[39] J. Wilkening, V. Vasan, Comparison of five methods of computing the Dirichlet–Neumann operator for the water wave problem, in: Nonlinear Wave Equations: Analytic and Computational Techniques, AMS, 2015.
[40] D.P. Nicholls, F. Reitich, Stability of high-order perturbative methods for the computation of Dirichlet-Neumann operators, J. Comput. Phys. 170 (2001) 276–298.
[41] V.E. Zakharov, Stability of periodic waves of finite amplitude on the surface of a deep fluid, Zhurnal Prikl. Mekh. Teckhnicheskoi Fiziki 8 (1968) 86–94.
[42] C.W. Curtis, S.S.P. Shen, Three-dimensional surface water waves governed by the forced Benney–Luke equation, Stud. Appl. Math. 135 (2015) 447–465.
[43] M. Derakhti, J.T. Kirby, Breaking-onset, energy and momentum flux in unsteady focused wave packet, J. Fluid Mech. 790 (2016) 553–581.
[44] S. Gavrilyuk, H. Kalisch, Z. Khorsand, A kinematic conservation law in free surface flow, Nonlinearity 28 (2015) 1805–1821.